Mathematical appendix:

Oligomerization and feedback on membrane recruitment stabilize PAR-3 asymmetries in *C. elegans* zygotes

Charles F. Lang, Alexander Anneken, Ondrej Maxian, and Edwin M. Munro

This part of the supplemental material deals with our mathematical model of PAR-3 kinetics, which is based strongly on previous work by some of us [10]. In our model, we let $A_n(x)$ be the density (number/length) of membrane-bound oligomers of size n at point x. The density of each oligomer size evolves according to the equations [10, Eq. (1)]

$$\partial_t A_1 = D_A \partial_x^2 A_1 + \left(k_A^{\mathrm{on}} + k_A^+ f_A^+(A)\right) A_{\mathrm{cyto}} - k_A^{\mathrm{off}} A_1 \tag{M1a}$$

$$+ 2k_A^{\mathrm{dp}} A_2 - 2k_A^{\mathrm{p}} A_1^2 + \sum_{n=3}^{N} \left(k_A^{\mathrm{dp}} A_n - k_A^{\mathrm{p}} A_1 A_{n-1}\right)$$

$$\partial_t A_n = k_A^{\mathrm{p}} A_1 \left(A_{n-1} - A_n\right) - k_A^{\mathrm{dp}} \left(A_n - A_{n+1}\right) \qquad N > n \geq 2 \tag{M1b}$$

$$\partial_t A_N = k_A^{\mathrm{p}} A_1 A_{N-1} - k_A^{\mathrm{dp}} A_N \tag{M1c}$$

$$A_{\mathrm{cyto}} = \frac{1}{hL}\left(A^{(\mathrm{Tot})} L - \int_0^L A(x)\, dx\right) \qquad A(x) = \sum_{n=1}^{N} n A_n(x). \tag{M1d}$$

A schematic diagram of this model can be found in Fig. 3A, and more details on its assumptions can be found in [10]. Briefly, the first line of (M1a) describes the evolution of monomers, which bind directly from the cytoplasm and unbind from the membrane in monomer form. The second line of (M1a), combined with (M1b) and (M1c) represent polymerization dynamics on the membrane. There the depolymerization rate k_A^{dp} is the rate at which oligomers of size n become oligomers of size $n - 1$. Because we assume oligomers are linear, this event can occur from either side, and as such the rate k_A^{dp} is twice that observed in single-molecule imaging. The cytoplasmic concentration is determined in (M1d) from the conservation of total protein in the system, where $A(x)$ is the total bound density at each point on the membrane.

1

The equations (M1) contain two important simplifying assumptions. First, our experimental data (Fig. 3K) shows that the unbinding kinetics of oligomers follows a power-law decay, with each additional monomer increasing the oligomer residence time by a factor of 4. Because of this, we neglect the unbinding of oligomers into the cytoplasm, as in [10]. Second, experiments have provided evidence for the direct positive feedback term $k_A^+ f_A^+(A)$. Previous simulations [10] have shown that direct binding and unbinding of cytoplasmic monomers to membrane-bound oligomers does not alter the qualitative behavior of the model (in terms of the types of steady states), but effectively weakens or strengthens the feedback strength depending on the regime considered. For this reason, we will not directly model the (un)binding of cytoplasmic monomers to membrane-bound oligomers, instead assuming that this is implicit in the feedback strength.

1 Nondimensionalization and parameter estimation

Because the total amount of PAR-3 in the system is unknown, and because each embryo has a slightly different length, it is necessary to scale the equations by appropriate time, length, and density scales. A sensible timescale for the system is the time a typical PAR-3 molecule spends on the membrane. Since polymerization dynamics are much slower than unbinding, this timescale is roughly $1/k_A^{\mathrm{dp}}$. We define the dimensionless (hatted) variables

$$x = \hat{x}L, \qquad t = \hat{t}/k_A^{\mathrm{dp}}, \qquad A = \hat{A}A^{(\mathrm{Tot})}.$$

Substituting into (M1) gives the rewritten dynamics [10, Eq. 14]

$$\partial_{\hat{t}}\hat{A}_1 = \hat{D}_A\partial_{\hat{x}}^2\hat{A}_1 + \hat{K}_A^{\mathrm{on}}\left(1 + \hat{K}_A^{\mathrm{f}}\hat{F}_A^+(\hat{A})\right)\left(1 - \int_0^1 \hat{A}(x)\,d\hat{x}\right) - \hat{K}_A^{\mathrm{off}}\hat{A}_1$$

$$+ 2\hat{A}_2 - 2\hat{K}_A^{\mathrm{p}}\hat{A}_1^{\,2} + \sum_{n=3}^{N}\left(\hat{A}_n - \hat{K}_A^{\mathrm{p}}\hat{A}_1\hat{A}_{n-1}\right) \tag{M2a}$$

$$\partial_{\hat{t}}\hat{A}_n = \hat{K}_A^{\mathrm{p}}\hat{A}_1(\hat{A}_{n-1} - \hat{A}_n) - (\hat{A}_n - \hat{A}_{n+1}) \qquad N > n \geq 2 \tag{M2b}$$

$$\partial_t\hat{A}_N = \hat{K}_A^{\mathrm{p}}\hat{A}_1\hat{A}_{N-1} - \hat{A}_N \tag{M2c}$$

$$\hat{D}_A = \frac{D_A}{L^2 k_A^{\mathrm{dp}}}, \quad \hat{K}_A^{\mathrm{on}} = \frac{k_A^{\mathrm{on}}}{k_A^{\mathrm{dp}}h}, \quad \hat{K}_A^{\mathrm{f}} = \frac{k_A^+ A^{(\mathrm{Tot})}}{k_A^{\mathrm{on}}}, \quad \hat{K}_A^{\mathrm{off}} = \frac{k_A^{\mathrm{off}}}{k_A^{\mathrm{dp}}}, \tag{M2d}$$

$$\hat{K}_A^{\mathrm{p}} = \frac{k_A^{\mathrm{p}} A^{(\mathrm{Tot})}}{k_A^{\mathrm{dp}}}, \quad \hat{F}_A^+(\hat{A}) = \frac{f_A^+(A)}{A^{(\mathrm{Tot})}}.$$

This study gives accurate measurements for three of the PAR-3-related parameters: the diffusion coefficient $D_A = 0.1~\mu\mathrm{m}^2/\mathrm{s}$, the detachment rate $k_A^{\mathrm{off}} = 3/\mathrm{s}$, and the *single molecule* depolymerization rate $0.08/\mathrm{s}$, which means that $k_A^{\mathrm{dp}} = 0.16/\mathrm{s}$. For lengthscales, a typical *C. elegans* embryo

has a roughly ellipsoidal shape, with half-axis lengths $27 \times 15 \times 15$ μm. As such, our model will be a 27×15 ellipse, which has perimeter $L = 134.6$ μm [6]. In our one-dimensional model, the cytoplasm has a "thickness" which is just the area of the ellipse 1272 μm^2 divided by the perimeter L, which gives $h = 9.5$ μm.

To fit the polymerization rate, we first solve (M2) at steady state to obtain an exponential distribution of oligomer sizes [4, 10]

$$\hat{A}_n = \hat{K}_A^{\mathrm{p}} \hat{A}_1 \hat{A}_{n-1} := \alpha \hat{A}_{n-1} \quad n \geq 2. \tag{M3}$$

This defines $\alpha = \hat{K}_A^{\mathrm{p}} \hat{A}_1$ as the coefficient of the exponential distribution of oligomer sizes. It follows that the total number of monomers is given by

$$\hat{A} = \sum_{n=1}^{N} n \alpha^{n-1} \hat{A}_1 \xrightarrow{N \to \infty} \frac{\hat{A}_1}{(1-\alpha)^2}. \tag{M4}$$

This equation can then be solved for $\hat{A}_1$ to obtain [10, Eq. (12)]

$$\hat{A}_1 = \frac{1 + 2\hat{A}\hat{K}_A^{\mathrm{p}} - \sqrt{1 + 4\hat{K}_A^{\mathrm{p}}\hat{A}}}{2\hat{A}\left(\hat{K}_A^{\mathrm{p}}\right)^2}, \tag{M5}$$

which gives the number of bound monomers (and therefore α) as a function of the total bound $\hat{A}$. To fit the value of $\hat{K}_A^{\mathrm{p}}$, we consider *spd-5* (RNAi) embryos, where the PAR-3 density is roughly uniform throughout the cortex. In these embryos (as with wild-type embryos), the level of protein in late maintenance phase is roughly half of the late-interphase levels. Thus, an upper bound on the bound density is $\hat{A} = 0.5$. Since the mean oligomer size is $\alpha \approx 0.7$, we obtain $\hat{K}_A^{\mathrm{p}} = 15$ as a reasonable parameter for the polymerization dynamics, since $\alpha\left(\hat{K}_A^{\mathrm{p}} = 15, \hat{A} = 0.5\right) = 0.7$.

2 The form of the feedback strength and resulting steady states

We now turn to models of feedback, which is the main focus of this supplement. Our goal in particular is to analyze the *stability* behavior with different feedback models, and use the qualitative behavior of the system to settle on (or at least strongly suggest) a preferred model. To do this, it will be vital to understand the behavior near steady state. In the absence of diffusion, invoking the steady state (M3) for polymerization dynamics reduces the monomer equation (M2a) to a balance of the binding flux (which combines the basal binding rate and the feedback) and the unbinding
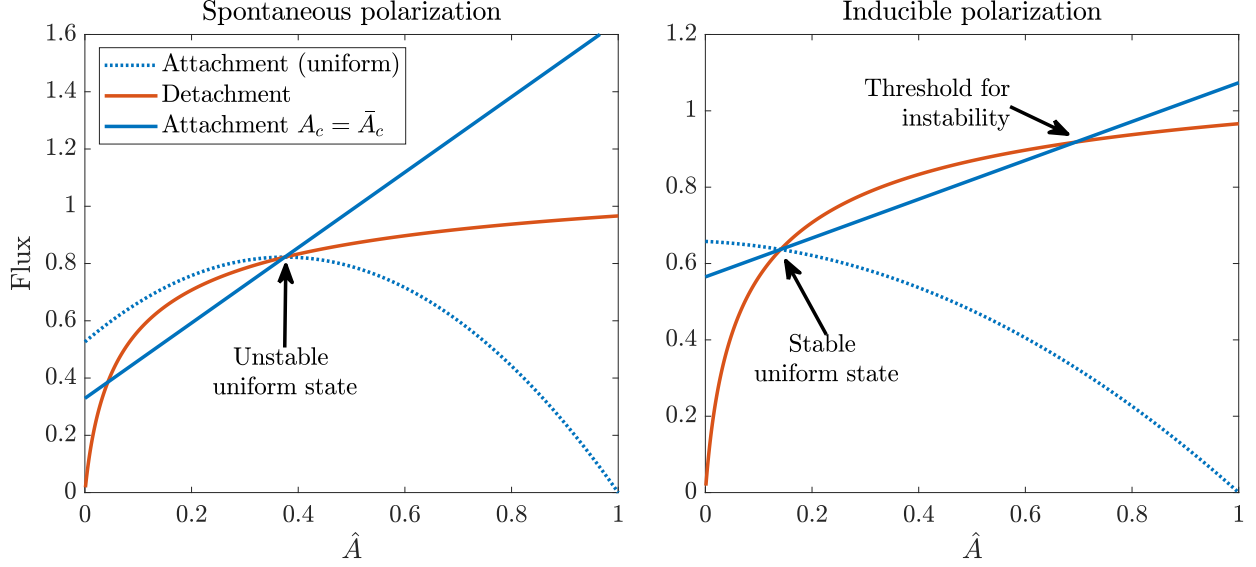
Figure M1: Flux plane analysis for linear feedback model (M7). The stability analysis is determined by how the attachment rate (solid blue line, with constant cytoplasmic concentration) compares to the detachment rate (red) near the steady state. In the left plot, the uniform state is unstable and spontaneous polarization is predicted, while in the right plot the uniform state is stable and polarization can be induced by large perturbations.

flux,

$$0 = \underbrace{\hat{K}_A^{\text{on}} \left(1 + \hat{K}_A^{\text{f}} \hat{F}_A^+(\hat{A}) \right) \hat{A}_c}_{\text{On flux}} - \underbrace{\hat{K}_A^{\text{off}} \hat{A}_1}_{\text{Off flux}} \tag{M6}$$

$$\hat{A}_c = \left(1 - \int_0^1 \hat{A}(x)\, d\hat{x} \right)$$

When the system is in a uniform state $\hat{A}(x) \equiv \hat{A}$, and the cytoplasmic concentration $\hat{A}_c = 1 - \hat{A}$, but this is not the case in polarized states. Thus when performing stability analysis, we need to consider *both* the case when $\hat{A}_c = 1 - \hat{A}$, and the case when it is constant and equal to its value at the uniform state (this corresponds to disregarding the flux law, as in local perturbation analysis [9]).

2.1 Linear feedback model

Let us first consider the linear feedback model that was used previously by some of us [10]

$$f_A^+(A) = A \rightarrow \hat{F}_A^+(\hat{A}) = \hat{A}. \tag{M7}$$

As shown in Fig. M1, the behavior of this model falls into one of two cases:

4

1. The uniform state is unstable. This occurs when the feedback dominates the basal binding rate.

2. The uniform state is stable, but it is possible to induce polarization by driving the local concentration above some threshold.

According to our experimental observations in *spd-5* (RNAi) embryos, the uniform state is in fact stable, which rules out scenario 1. Thus, we choose parameters that fall in the regime of scenario 2. Here we are strongly constrained by the fact that the anterior state (in wild-type) closely resembles the uniform state (*spd-5* (RNAi)), so the threshold for instability must lie close to the unstable uniform state. In Fig. M2(a), we show the flux plane for a set of parameters ($\hat{K}_A^{\mathrm{on}} = 0.7$ and $\hat{K}_A^{\mathrm{f}} = 1.6$) where this is the case.

The dynamics that result are shown in Fig. M2(b). In the left panel, we see that perturbations to the uniform state are stable, which matches the observations in *spd-5* embryos. In the right panel, we see that polarized states are self-sustaining. The polarized state shown there initially shrinks down in both the "posterior" and "anterior" sides, reaching a quasi-stable state between $t = 5$ and $t = 20$ minutes. Then, as expected from our flux analysis, the anterior concentration grows and the posterior concentration shrinks, as there is nothing to stop the instability from growing. The timescale on which this occurs, however, is about 30 minutes (resulting from slow oligomerization dynamics), which is much longer than maintenance phase in live embryos.

Because of this important fact, it is impossible to say for certain that the linear feedback model is incorrect, though its tendency to focus the anterior cap is concerning. One hint we do get, however, is the key separation between the uniform state ($\hat{A} \approx 0.2$) and the enriched anterior state ($\hat{A} \approx 0.6$). This is a consequence of the model we have chosen; because the "anterior" state lies above an unstable fixed point which is in turn above the uniform steady state, there has to be a good deal of space between the two points. This is *not* what we see in our embryos, where we observe a good match between the uniform state and anterior state.

2.2 Saturated feedback model with bistability

The data consequently argue for an alternative model where the uniform state is a stable state that could coexist with a depleted posterior state for certain values of the feedback strength. In this case, rather than driving the anterior side above the uniform state, we would attain polarization by driving the posterior state down to a new stable state.
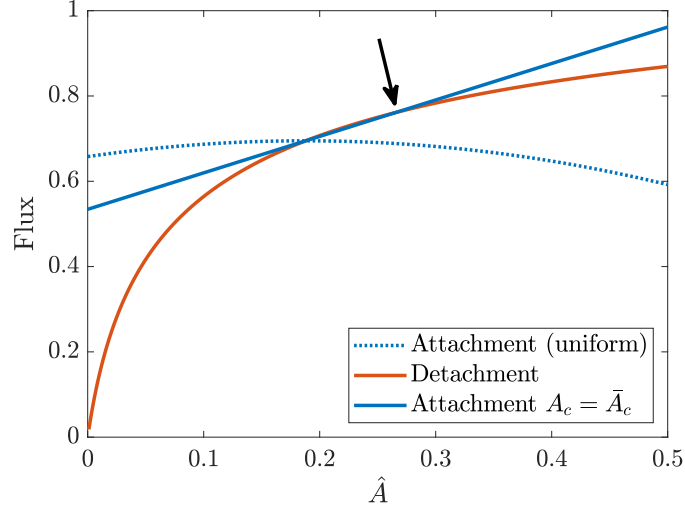
(a) Flux plane
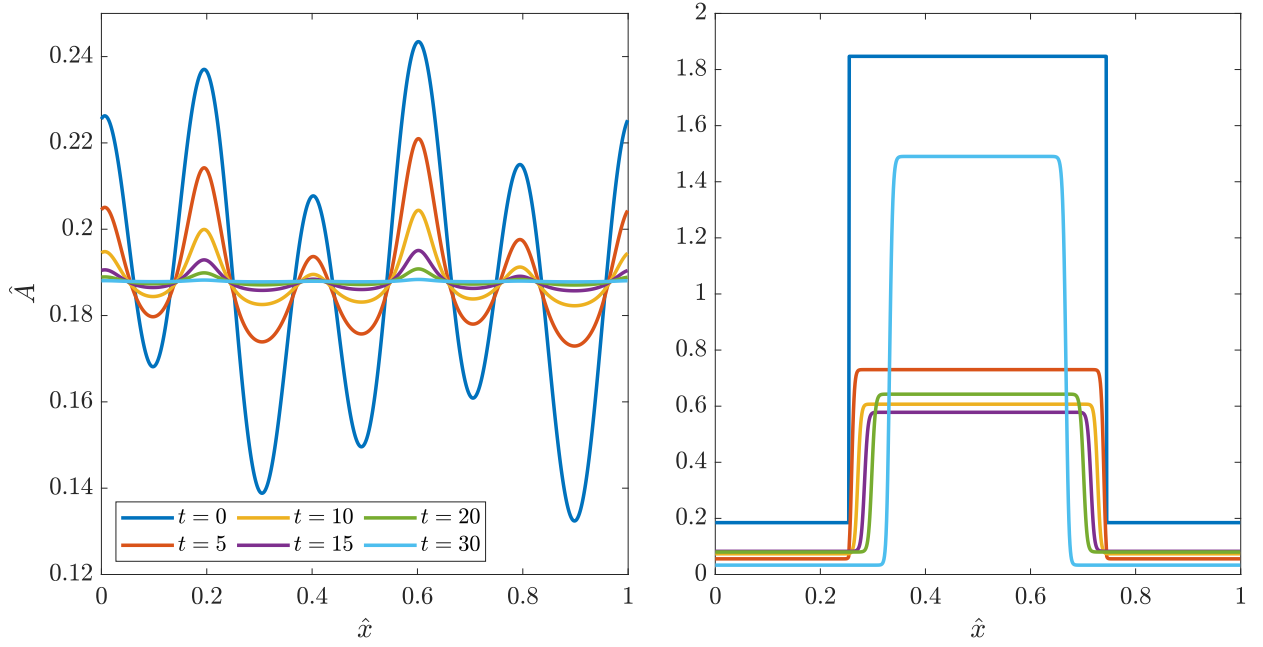
(b) Dynamics

Figure M2: Linear feedback model with our chosen parameters, $\hat{K}_A^{\mathrm{on}} = 0.7$ and $\hat{K}_A^{\mathrm{f}} = 1.6$. (a) Flux plane analysis. The uniform state is linearly stable, but perturbations (beyond the black arrow) can induce polarized states. (b) Dynamic trajectories starting from a perturbed uniform state (left), and a polarized state (right). Time is marked in minutes.

In order for this scenario to play out, the attachment flux at constant cytoplasmic concentration has to intersect the detachment curve three times (two stable fixed points and one unstable fixed point in between), which is impossible with a linear feedback function. A simple way to accomplish this is by introducing saturation into the feedback curve,

$$f_A^+(A) = \min\left(A, A^{(\text{Sat})}\right) \rightarrow \hat{F}_A^+(\hat{A}_1, \hat{A}_n) = \min\left(\hat{A}, \hat{A}^{(\text{Sat})}\right). \tag{M8}$$

As shown in the flux balance plot in Fig. M3(a), the uniform state is stable if the feedback saturates *below* the uniform state concentration. Indeed, if the feedback saturated above the uniform state, then we would once again have linear feedback near the uniform state, which is a regime we are trying to move away from.

The saturation point $\hat{A}^{(\text{Sat})}$ is another parameter that we must constrain. While the feedback cannot saturate above the uniform state, it also cannot saturate too far below the uniform state, since then it could be folded into the basal binding rate, making sustained polarization impossible. For this reason, we choose to saturate the feedback at 80% of the uniform state, regardless of the other parameters. Once this saturation threshold is set, we choose the basal bind rate $\hat{K}_A^{\text{on}} = 0.7$ (same as in linear feedback model) and the feedback strength $\hat{K}_A^{\text{f}} = 3.6$ to produce the flux balance plot in Fig. M3(a). Such a choice gives a uniform/anterior state around $\hat{A} \approx 0.45$ and a posterior state which coexists around $\hat{A} = 0.05$.

The dynamics of this model are shown in Fig. M3(b). As with the linear feedback model, we observe stability of the uniform state, and a polarized state which is self-sustaining. Two key features distinguish the model with saturation: first, the polarized state is stable, in the sense that waiting infinite time would not produce contraction and focusing of the anterior domain. Second, the polarized anterior state is significantly closer to the uniform state; since the uniform and anterior states correspond to the same point on the flux balance plot, the differences between them are driven by changes in cytoplasmic concentration, as opposed to the need to induce polarization by driving the anterior side above a threshold higher than the uniform state. These two reasons are why we favor the feedback model with saturation over the simpler linear feedback model.

2.2.1 Phase diagram

We now use local perturbation analysis to prepare a phase diagram of the stability behavior for our saturated feedback model. To do so, we set the parameters $\hat{K}_A^{\text{p}}$ and $\hat{K}_A^{\text{f}}$, and plot the flux balance diagram shown in Fig. M3(a). In local perturbation analysis, we disregard the flux law, so that the
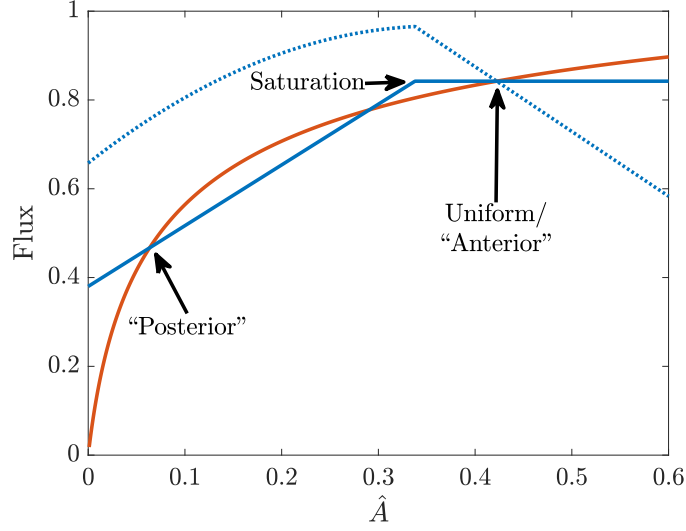
(a) Flux plane
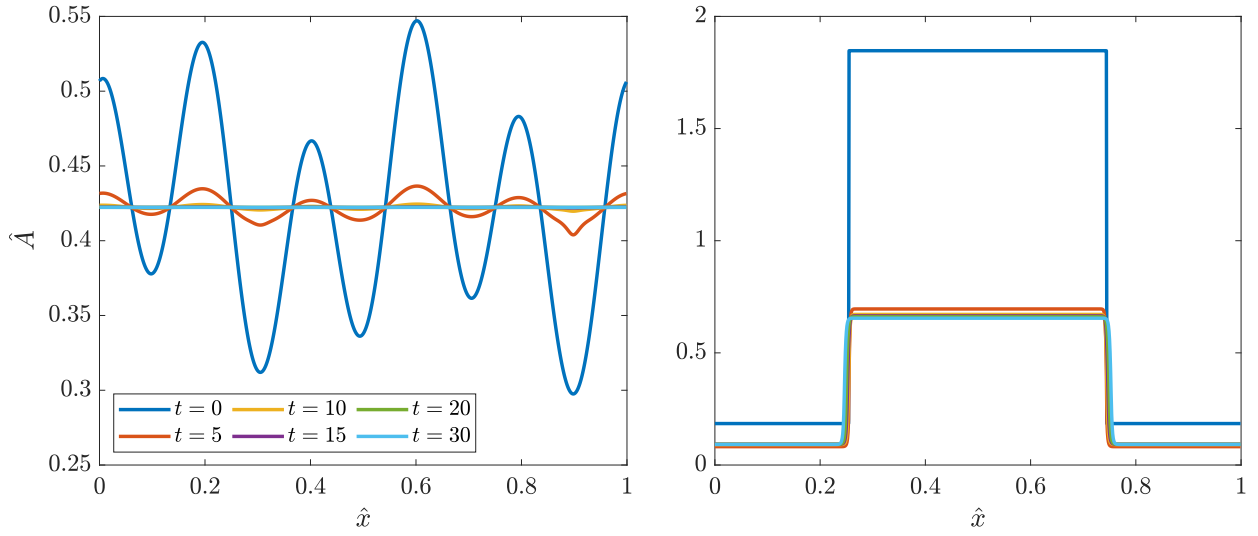
(b) Dynamics

Figure M3: Steady state analysis for capped linear feedback in the bistable case ($\hat{K}_A^{\mathrm{on}} = 0.66$ and $\hat{K}_A^{\mathrm{f}} = 3.6$). Left plot: The stability analysis is determined by how the attachment rate (solid blue line, with constant cytoplasmic concentration) compares to the detachment rate (red) near the steady state. The uniform state ($\hat{A}_u \approx 0.4$) is stable, and coexists with a depleted state. Right plot: the stable polarized state that results when we perturb away from the uniform state with these parameters.

Parameter	Description	Value	Units	Ref	Notes
L	Domain length	134.6	μm	[6]	radii 27×15 μm ellipse
h	Cytoplasmic "thickness"	9.5	μm	[6]	(area/circumference)
D_A	Monomeric PAR-3 diffusivity	0.1	$\mu m^2/s$		This study
k_A^{on}	Monomeric PAR-3 attachment rate	1	$\mu m/s$		Fitting
k_A^{off}	Monomeric PAR-3 detachment rate	3	$1/s$		This study, Fig. 3K
k_A^{dp}	PAR-3 depolymerization rate	0.16	$1/s$		This study, Fig. 4E
$\hat{K}_A^{\mathrm{p}}$	PAR-3 polymerization rate	15			Fit α in uniform state
N	Max oligomer size	50			Same results for larger N
$A^{(\mathrm{Tot})}$	Maximum bound PAR-3 density	–	$\#/\mu m$		Contained in other unknowns

Table 1: Parameter values for the PAR-3 model (see (M2d) for the definitions of dimensionless parameters). Here we leave out the feedback parameter $\hat{K}_A^{\mathrm{f}}$, which varies depending on the model being considered.

behavior of the system is controlled by the solid blue (attachment) and red (detachment) lines in Fig. M3(a). For each set of parameters, the uniform state is stable by construction, and we need only check if there is another stable depleted state. If there is, we have bistability, and we record the A/P ratio predicted by the flux balance plot. In Fig. M4, we plot the phase diagram for mean oligomer size (at the uniform/anterior state) vs. the feedback strength. Red dots show parameters where the uniform state is stable, while colors on the colorbar have stable A/P ratios larger than unity. We notice how the balance between feedback and oligomerization sets the boundary; when the oligomerization strength is higher, less direct feedback is needed to generate bistability.

2.3 Systematic depletion of PAR-3

We now model the experiment of PAR-3 depletion, where RNAi removes a fraction of the total PAR-3 from the system, giving a remaining fraction

$$F = A^{(\mathrm{Tot})}/A_{\mathrm{WT}}^{(\mathrm{Tot})}.$$

of the wild type. Given the base values that we have already fit in wild type embryos, the scalings in (M2d) clearly show how the dimensionless parameters $\hat{K}_A^{\mathrm{p}}$ (polymerization) and $\hat{K}_A^{\mathrm{f}}$ (feedback strength) should scale with F, which fixes all of the parameters in our simulations. To simulate experimental conditions for a given F, we start at the end of establishment phase, which corresponds to all protein bound to the membrane and a roughly 10:1 ratio of anterior to posterior protein (this the dark blue protein profile in the right panel of Figs. M2(b) and M3(b)). We then run forward

9
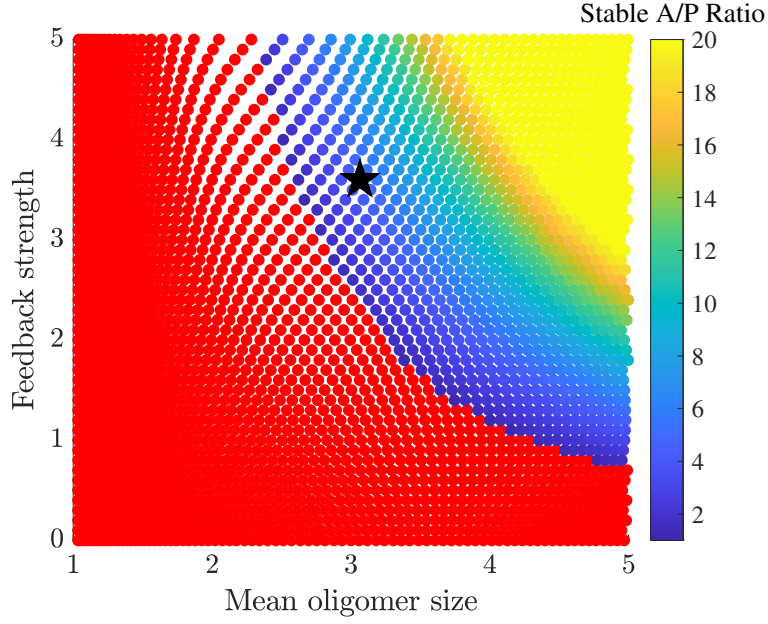
Figure M4: Phase diagram for bistability of PAR-3 asymmetries. We show steady states with various mean oligomer sizes on the anterior and differing feedback strengths $\hat{K}_A^{\mathrm{f}}$, where the saturation point scales so that the uniform steady state is stable for all choices of parameters. The red circles show the region of parameter space with a single stable state, while the blue–yellow circles show the region of bistability (color-coded based on the size of the A/P asymmetry). The black star denotes the parameters in the wild-type embryo.
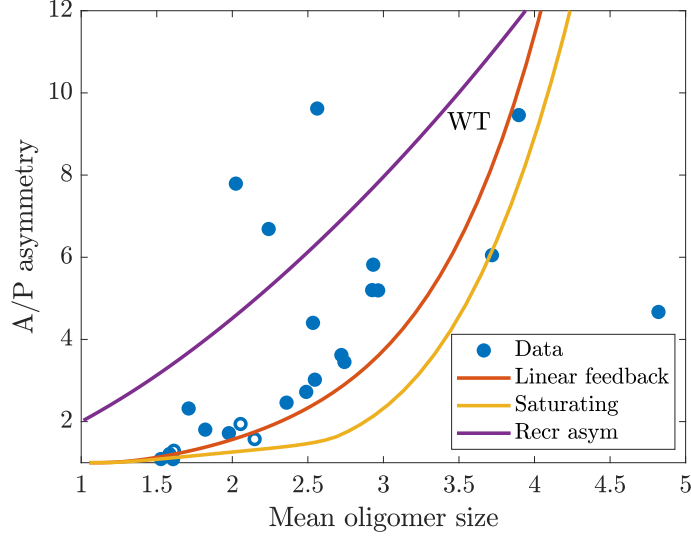
Figure M5: Dynamic PAR-3 depletion experiment. For different fractions of the wild-type PAR-3 concentration, we initialize the domain with a 10:1 asymmetry (50% enriched and 50% depleted) and watch the evolution over four minutes with three different feedback models. The red line shows results with the linear feedback model, while the yellow line shows results with the saturating feedback model. The purple line shows results for an alternative model based on asymmetric recruitment of monomers to the membrane.

in time until we reach $t = 4$ minutes ($\hat{t} = 38.4$), corresponding exactly to the time interval used in experiments. At this time, we record the mean oligomer size

$$\left(\sum_{n=1}^{N} n \hat{A}_n \right) \Big/ \left(\sum_{n=1}^{N} \hat{A}_n \right)$$

on the anterior, and the A/P ratio.

Figure M5 shows the results for our different feedback models compared to experimental data. At the level of this experiment, it is not possible to distinguish between the linear feedback and saturating feedback models, since they both produce qualitatively the same results, with slight shifts in the curves due to parameterization. Specifically, both of these models predict that there is a minimum oligomer size needed to sustain A/P asymmetries. This is in contrast to a model based on asymmetric recruitment (in which case there is no feedback and monomers are recruited to the anterior at twice the rate of the posterior), which predicts a persistent asymmetry even as the mean oligomer size drops to 1 (i.e., even without oligomerization). While this experiment cannot distinguish the type of feedback, it makes clear that positive feedback, and not asymmetric recruitment, drives persistent asymmetries in protein concentration.
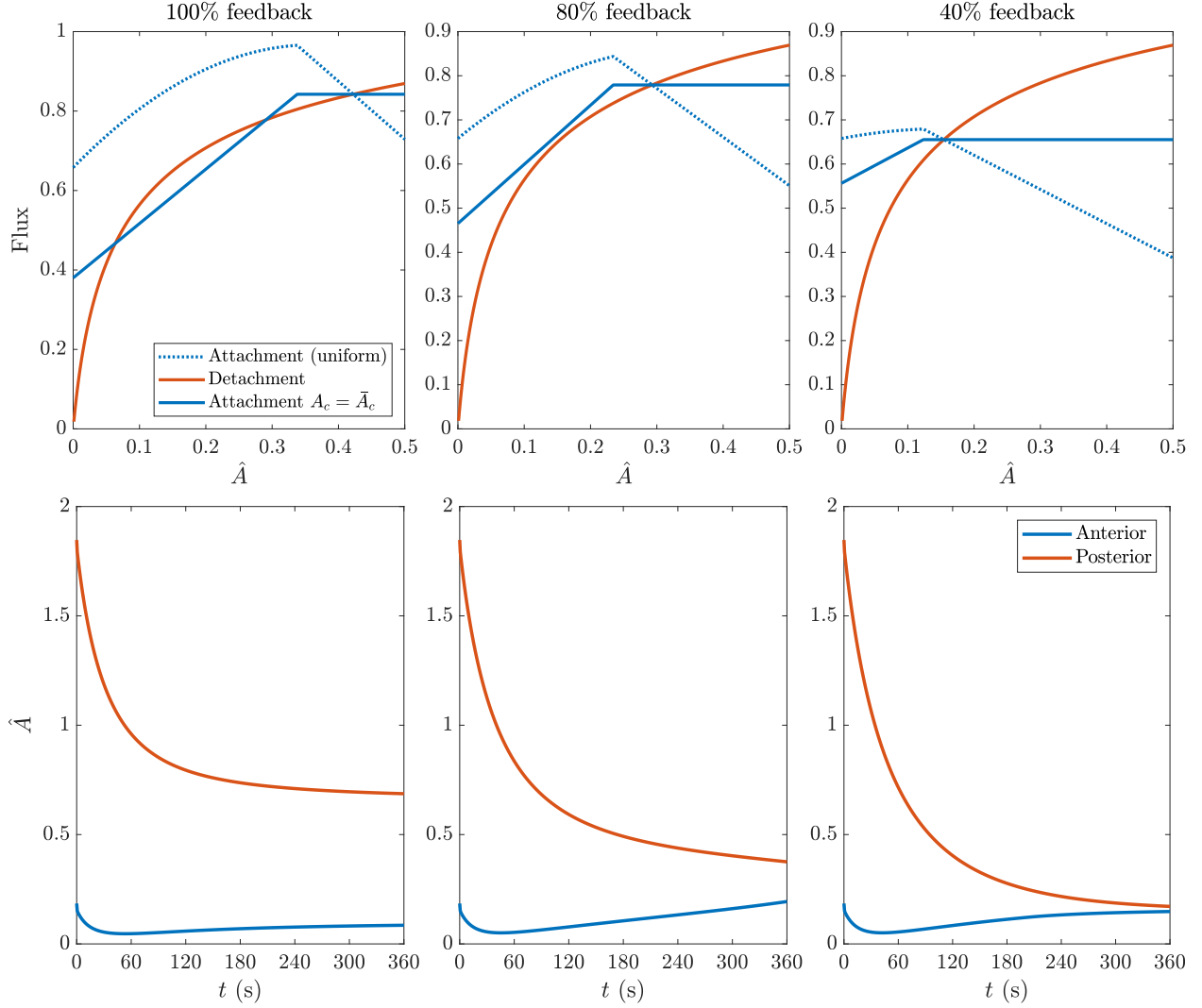
2.4 Reducing feedback

Finally, we use our saturated feedback model to demonstrate what might happen when the feedback is reduced, in order to explain the results of some of our perturbation experiments. In Fig. M6, we consider three different feedback strengths: 100% feedback ($\hat{K}_A^{\mathrm{f}} = 3.6$), 80% ($\hat{K}_A^{\mathrm{f}} = 2.9$) and 40% ($\hat{K}_A^{\mathrm{f}} = 1.4$). In the top plots, we show the flux balance plots near the uniform state. When the feedback is weakened, there is a loss of local bistability, and thus only a single steady state (the uniform state). We observe the resulting dynamics in the bottom set of plots, where we plot the evolution of asymmetries (set over 50% of the domain) over time for the three different feedback strengths. At the base parameter set, the posterior domain retains its original low value, and the anterior drops from its peak at late establishment, but maintains the asymmetries. When the feedback is reduced by 20%, the uniform steady state is higher than the original posterior state, and so the posterior domain concentration increases to meet the dropping anterior domain concentration (this is similar to the results for CDC-42 (RNAi) in Fig. 6D). Finally, when the feedback is strongly reduced, the uniform state becomes about the same as the original posterior state, and the dynamics we observe are just the anterior state dropping to meet the posterior (this is similar to what we observe in PAR-6 (RNAi) in Fig. 6D).

3 Some text for conclusions

Unlike in budding yeast cells [11], there is no experimental evidence that *C. elegans* cells can spontaneously polarize, which means that the system is truly bistable. Traditionally, it has been speculated that the bistability comes from mutual inhibition of the aPAR and pPAR proteins [8, 14]. But translating this idea into equations becomes much harder than might be expected! Indeed, ODEs based on first-order mass action kinetics of aPAR-pPAR inhibition *do not* yield bistable dynamics under any choice of parameters [2]. Attempts to overcome this have used stoichiometric coefficients for the biochemical equations that guarantee bistability [6, 7] or included actomyosin flows designed to transport the aPARs only [13].

The experimental observations in this study provide a potential way out of this conundrum. It has long been known that disrupting PAR-3 [5] or its oligomerization [3] leads to a failure or severe disruption in establishing polarity. But our finding that PAR-3 asymmetries are stable even in the absence of posterior inhibitor PAR-1 [12] demonstrates that the dynamics of PAR-3 *by itself* are intrinsically bistable, and might therefore "anchor" the bistability of the entire

Figure M6: How the system responds to reductions in feedback. In the top plots, we show the theoretical flux balance when considering 100% feedback ($\hat{K}_A^{\mathrm{f}} = 3.6$), and then reducing the feedback strength by 20% ($\hat{K}_A^{\mathrm{f}} = 2.9$) and 60% ($\hat{K}_A^{\mathrm{f}} = 1.4$). Bottom plots: we show the trajectory of the anterior (red) and posterior (blue) concentration over five minutes using these two feedback strengths.

PAR protein system. Our model therefore distinguishes itself from that of [10] by arguing for *bi*stability (described previously as "inducible polarization") rather than spontaneous *in*stability. The requirement for this bistability is that the "feedback" (recruitment of cytoplasmic monomers to the membrane by membrane-bound ones) must saturate at a point below the steady state, a regime which experimental observations strongly suggest the system operates in.

Given the intrinsic bistability of PAR-3, an exciting future direction is to introduce additional biochemistry and contractility into the model [12], and see if it can reproduce a stable boundary position under these circumstances. Because of the intrinsic bistability of PAR-3, we expect that first-order inhibition dynamics will be enough to generate bistability, which is in contrast to previous studies which did not account for the positive feedback of membrane-bound monomers promoting binding of cytoplasmic ones [2]. While this model is not meant to exclude other possible nonlinearities in the reaction kinetics [1], it does show that they are not strictly necessary for stable polarization.

References

[1] Tom Bland, Nisha Hirani, David Briggs, Riccardo Rossetto, KangBo Ng, Neil Q McDonald, David Zwicker, and Nathan W Goehring. Optimized dimerization of the par-2 ring domain drives cooperative and selective membrane recruitment for robust feedback-driven cell polarization. *bioRxiv*, pages 2023–08, 2023.

[2] Adriana T Dawes and Edwin M Munro. Par-3 oligomerization may provide an actin-independent mechanism to maintain distinct par protein domains in the early caenorhabditis elegans embryo. *Biophysical journal*, 101(6):1412–1422, 2011.

[3] Daniel J Dickinson, Francoise Schwager, Lionel Pintard, Monica Gotta, and Bob Goldstein. A single-cell biochemistry approach reveals par complex dynamics during cell polarization. *Developmental cell*, 42(4):416–434, 2017.

[4] Leah Edelstein-Keshet and G Bard Ermentrout. Models for the length distributions of actin filaments: I. simple polymerization and fragmentation. *Bulletin of mathematical biology*, 60(3):449–475, 1998.

[5] Bijan Etemad-Moghadam, Su Guo, and Kenneth J Kemphues. Asymmetrically distributed par-3 protein contributes to cell polarity and spindle alignment in early c. elegans embryos. *Cell*, 83(5):743–752, 1995.

[6] Nathan W Goehring, Philipp Khuc Trong, Justin S Bois, Debanjan Chowdhury, Ernesto M Nicola, Anthony A Hyman, and Stephan W Grill. Polarization of par proteins by advective triggering of a pattern-forming system. *Science*, 334(6059):1137–1141, 2011.

[7] Peter Gross, K Vijay Kumar, Nathan W Goehring, Justin S Bois, Carsten Hoege, Frank Jülicher, and Stephan W Grill. Guiding self-organized pattern formation in cell polarity establishment. *Nature physics*, 15(3):293–300, 2019.

[8] Jacob Halatek, Fridtjof Brauns, and Erwin Frey. Self-organization principles of intracellular pattern formation. *Philosophical Transactions of the Royal Society B: Biological Sciences*, 373(1747):20170107, 2018.

[9] William R Holmes, May Anne Mata, and Leah Edelstein-Keshet. Local perturbation analysis: a computational tool for biophysical reaction-diffusion models. *Biophysical journal*, 108(2):230–236, 2015.

[10] Charles F Lang and Edwin M Munro. Oligomerization of peripheral membrane proteins provides tunable control of cell surface polarity. *Biophysical Journal*, 121(23):4543–4559, 2022.

[11] Alex Mogilner, Jun Allard, and Roy Wollman. Cell polarity: quantitative modeling as a tool in cell biology. *Science*, 336(6078):175–179, 2012.

[12] Anne Sailer, Alexander Anneken, Younan Li, Sam Lee, and Edwin Munro. Dynamic opposition of clustered proteins stabilizes cortical polarity in the c. elegans zygote. *Developmental cell*, 35(1):131–142, 2015.

[13] Filipe Tostevin and Martin Howard. Modeling the establishment of par protein polarity in the one-cell c. elegans embryo. *Biophysical journal*, 95(10):4512–4522, 2008.

[14] Philipp Khuc Trong, Ernesto M Nicola, Nathan W Goehring, K Vijay Kumar, and Stephan W Grill. Parameter-space topology of models for cell polarity. *New Journal of Physics*, 16(6):065009, 2014.